ARTICLE

Binary Pt–Si Nanostructures Prepared by Focused Electron-Beam-Induced Deposition

Marcel Winhold,[†,⊥] Christian H. Schwalb,[†,⊥] Fabrizio Porrati,[†] Roland Sachser,[†] Achilleas S. Frangakis,[‡] Britta Kämpken,[§] Andreas Terfort,[§] Norbert Auner,[§] and Michael Huth[†,*]

[†]Physikalisches Institut, [‡]Institut für Biophysik, and [§]Institut für Anorganische und Analytische Chemie, Goethe Universität, 60438 Frankfurt am Main, Germany. [⊥]These authors contributed equally to this work.

ABSTRACT Binary systems of Pt–Si are prepared by electron-beam-induced deposition using the two precursors, trimethyl(methylcyclopentadienyl)platinum(IV) ($MeCpPt(Me)_3$) and neopentasilane ($Si(SiH_3)_4$), simultaneously. By varying the relative flux of the two precursors during deposition, we are able to study composites containing platinum and silicon in different ratios by means of energy-dispersive X-ray spectroscopy, atomic force microscopy, electrical transport measurements, and transmission electron microscopy. The results show strong evidence for the formation of a binary, metastable Pt_2Si_3 phase, leading to a maximum in the conductivity for a Si/Pt ratio of 3:2.

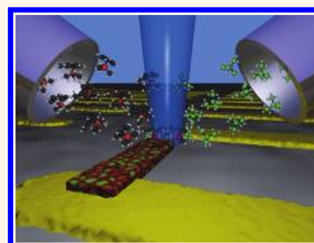

KEYWORDS: focused electron-beam-induced deposition · binary systems · platinum silicides · nanogranular materials · electronic transport · nanostructures

In recent years, focused electron-beam-induced deposition (FEBID) has shown impressive development as a micro- and nanofabrication tool. The proven applications range from photomask repair,[1] single-crystal nanowires,[2] and nanopores[3] to magnetic sensors[4−6] or tunable strain sensors.[7] The maskless bottom-up technique can be applied to nearly all surfaces and allows for an easy downscaling of structures to below 20 nm.

The structures prepared by the FEBID process are for many cases and for a large variety of the used precursors nanogranular. They consist of metallic nanocrystallites embedded in a carbon-rich dielectric matrix. In general, granular metals are ideal candidates for the study of fundamental aspects such as cooperative effects in the presence of disorder, electron correlations, reduced dimensionality, and quantum size effects.[8] Prominent fields of work using granular metals address the correlation-driven metal–insulator transition under variation of the intergrain coupling strength[9−14] or metallic volume fraction[15] and the study of cooperative ground states, such as superconductivity and magnetism.[16−18]

For the FEBID process, typically a single precursor gas is used in order to create a solid deposit by dissociation of the precursor molecules that are adsorbed on the substrate. In this work, we expand the standard FEBID approach to binary systems. This technique extends the base of accessible materials to a large degree and in addition offers a pathway for the formation of materials far away from thermal equilibrium conditions, therefore enabling the formation of metastable phases that are not accessible by standard deposition techniques.

One particular interesting material class of binary systems is the metal silicides, including platinum silicides. They are an integral part of all microelectronic devices and have been used for a long time in integrated circuit (IC) processing.[19,20] In the present work, we simultaneously used the widely known precursor trimethyl(methylcyclopentadienyl)platinum(IV) ($MeCpPt(Me)_3$) and neopentasilane ($Si(SiH_3)_4$), a substance which has not been used for FEBID yet. We systematically studied the properties of deposits of different Pt–Si composition formed under highly non-equilibrium growth conditions as is typical for FEBID. The deposits were measured by atomic force microscopy (AFM) in order to determine the growth rate for the different Si/Pt ratios. We observe a nonmonotonic growth rate with a maximum for a Si/Pt ratio of 0.8:1. We also performed *in situ* and temperature-dependent electrical transport measurements. The latter indicate a Mott-type variable range hopping (VRH) for samples with either high or low silicon content, while samples with a Si/Pt ratio of 1:1 and 3:2 show correlated VRH. Microstructural

* Address correspondence to michael.huth@physik.uni-frankfurt.de.

Received for review August 16, 2011 and accepted November 3, 2011.

Published online November 03, 2011
10.1021/nn203134a

© 2011 American Chemical Society

analysis of the deposits using high-resolution cross-section transmission electron microscopy (TEM) in combination with diffraction measurements revealed a decrease of crystallinity for the nanogranular platinum crystals with increasing silicon content in the deposits. The decrease in crystallinity and the drop in resistivity found for samples of 1:1 and 3:2 Si/Pt ratio suggest that a major part of the platinum atoms participates in the formation of a binary, amorphous Pt−Si phase.

RESULTS

Characterization of Deposits. After the deposition by FEBID as well as after the samples were exposed to air, an energy-dispersive X-ray spectroscopy (EDX) analysis was carried out for all samples in order to analyze the composition of the different deposits. Figure 1 displays the percentage of platinum, silicon, carbon, and oxygen in atom % by sample number. The results are summarized in Table 1. Sample 1 represents the Pt−C reference that was deposited without $Si(SiH_3)_4$ precursor flux. It contains 22% platinum and 78% carbon. For all following samples (2−9), we simultaneously introduced the precursors $MeCpPt(Me)_3$ and $Si(SiH_3)_4$ into the chamber and increased the $Si(SiH_3)_4$ precursor flux for every new deposit. The $MeCpPt(Me)_3$ precursor flux was kept fixed. This method allowed us to precisely tune the silicon content in the samples. Figure 1a displays the composition of the deposits directly after deposition. With increasing $Si(SiH_3)_4$ precursor flux, we observe an increasing silicon content starting from 3.8% for sample 2 up to 35.6% for sample 9, while the carbon and platinum content continuously decrease to 47.2 and 12.7%, respectively. Furthermore, in contrast to sample 1, all Pt−Si deposits contain 3−5% oxygen, presumably due to reactions with the residual gas, whose main contribution is H_2O as is typically the case under high-vacuum conditions.

In Figure 1b, the composition of all samples after exposure to air is shown. The samples show an increased oxygen content reaching a maximum of 24.7% for sample 5. This increase can be attributed to two mechanisms: First, oxygen can be embedded into the porous carbon matrix[9] of the silicon-free Pt−C deposit (sample 1). This eventually leads to an oxygen content of 12.4% even for the silicon-free sample 1. Second, the oxidation of silicon preferentially leads to SiO or SiO_2. The greater relative amount of oxygen in the deposits is achieved at the expense of carbon and silicon, whereas the change of the platinum content with a maximum difference of 3% compared to the composition directly after deposition is relatively small. Starting from sample 1, the carbon content decreases to 43.7% for sample 5 and remains constant for all samples with higher silicon content.

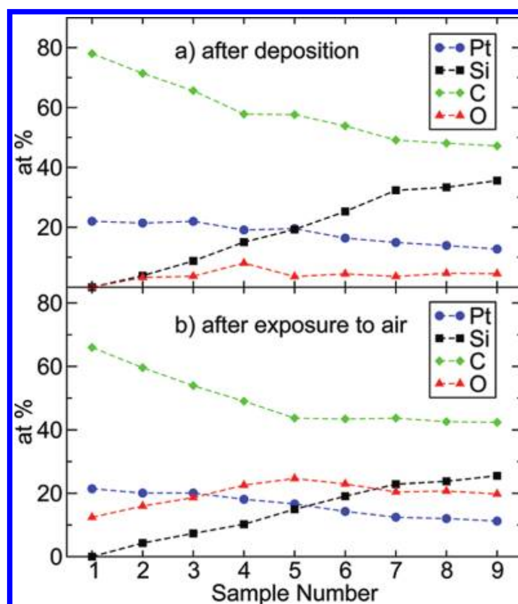

Figure 1. EDX measurements for all samples displaying the composition of platinum (circles), silicon (squares), carbon (diamonds), and oxygen (triangles) of all deposits (a) directly after the deposition and (b) after the electrical transport measurements and exposure to air.

The resistivity was determined from *I*−*V* characteristics taking into account the size of the deposits as obtained from SEM inspection and AFM height measurements. Figure 2 shows the measured heights for all deposits having equal lateral dimensions ($1 \times 6\ \mu m^2$). We observe a nonmonotonic growth rate as a function of silicon content. Starting from the silicon-free deposit (sample 1), the growth rate first increases with growing silicon content. The growth rate exhibits a distinct maximum for sample 4 corresponding to a Si/Pt ratio of 0.8:1. Further increasing the silicon content leads to a subsequent decrease in the deposits' height resulting in a growth rate for sample 9 that is more than 30% lower as compared to the Pt−C reference.

Figure 3 displays the resistivity directly after the deposition as well as after the electrical transport measurements and exposure of the samples to air. Starting from the silicon-free Pt−C deposit (sample 1), the resistivity decreases by almost 2 orders of magnitude, leading to a distinct minimum for a silicon content of 25.3% (sample 6). This corresponds to a ratio of Si/Pt of 3:2. For larger silicon content, the resistivity increases again. The resistivity curve progression of the air-exposed deposits basically shows an analogous behavior with a slight increase of resistivity for all samples due to aging effects. The Pt−C reference (sample 1) displays a much stronger aging effect under exposure to air, leading to a decrease in resistivity. The aging process of FEBID structures, in general, and the related reduction of conductivity are well-known and were also found for platinum- and tungsten-based deposits during exposure to air.[21,22] However, the exact mechanisms that are responsible for the aging characteristics in the Pt−Si

TABLE 1. Composition of the Different Samples and Calculated Si/Pt Ratio Directly after the Deposition (Left Column) and after Exposure to Air (Right Column) Measured with EDX[a]

	after deposition					after exposure to air				
sample	Si (atom %)	Pt (atom %)	C (atom %)	O (atom %)	Si/Pt	Si (atom %)	Pt (atom %)	C (atom %)	O (atom %)	Si/Pt
1	0.0	22.0	78.0	0.0	0.0	0.0	21.5	66.1	12.4	0.0
2	3.8	21.4	71.6	3.2	0.2	4.3	20.1	59.6	16.0	0.2
3	8.8	22.0	65.5	3.7	0.4	7.3	20.1	54.0	18.6	0.4
4	15.1	19.1	57.8	8.0	0.8	10.2	18.2	49.0	22.6	0.6
5	19.3	19.6	57.6	3.5	1.0	15.0	16.6	43.7	24.7	0.9
6	25.3	16.4	53.8	4.5	1.5	19.1	14.3	43.6	23.0	1.3
7	32.4	14.9	49.1	3.6	2.2	23.0	12.5	44.0	20.5	1.8
8	33.4	13.9	48.0	4.7	2.4	24.0	12.1	43.0	20.9	2.0
9	35.6	12.7	47.2	4.5	2.8	25.8	11.4	42.8	20.0	2.3

[a] The deposition parameters were identical for all samples (beam energy = 5 keV; beam current = 930 pA; pitch = 20 nm; dwell time = 1 μs). Sample 1 represents the silicon-free Pt–C reference, whereas samples 2–9 have an increasing Si/Pt ratio.

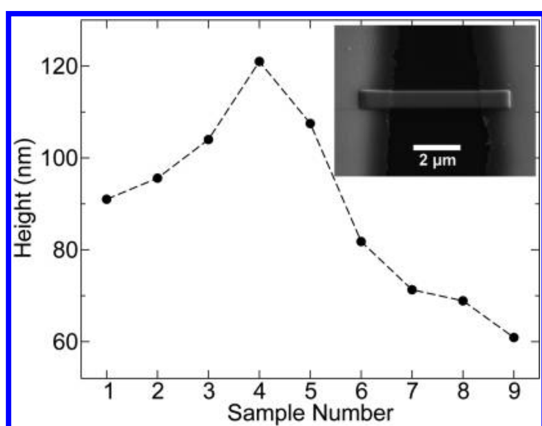

Figure 2. Height of all samples measured with AFM. A nonmonotonic growth rate as a function of silicon content can be observed with a clear maximum in the growth rate for a Si/Pt ratio of 0.8:1. Inset: Representative SEM image of a deposit grown by FEBID on a p-doped silicon substrate with a 300 nm thermal oxide layer for electrical insulation between 120 nm thick Cr/Au contacts. Beam current 930 pA, acceleration voltage 5 kV, lateral dimensions 1 × 6 μm^2, pitch 20 nm, dwell time t_D = 1 μs, and deposition time Δt = 60 s were kept fixed for all deposits.

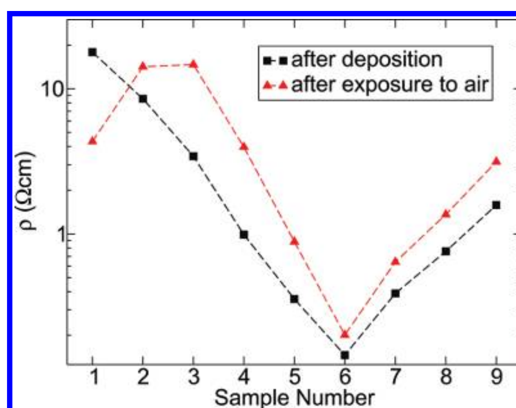

Figure 3. Resistivity, ρ, for all samples after deposition (squares) and after exposure to air (triangles). For sample 6, ρ exhibits a distinct minimum. The resistivity curve progression of the air-exposed deposits basically shows an analogous behavior with a slight increase of resistivity for all samples due to aging effects. The Pt–C reference (sample 1) shows a different aging behavior leading to a reduction of ρ.

compounds are not yet completely understood and need to be addressed in further experiments.

Electrical Transport Measurements. In Figure 4, an overview of the measured temperature-dependent conductivity for selected samples with representative Si/Pt ratios is given. The conductivity data for every deposit are shown normalized to the corresponding value at 260 K. In the inset of Figure 4, the absolute values of the temperature-dependent resistivity are shown for the same samples. All samples show a rapid decrease of conductivity as the temperature is lowered. Even sample 6 that has the nominal highest conductivity shows insulating behavior below ~20 K.

In order to gain a deeper insight into the actual electron transport mechanisms, Figure 5 displays the electrical conductivity plotted logarithmically *versus* (a) $T^{-1/2}$ and (b) $T^{-1/4}$ for selected samples. The data are plotted for values of σ for which the measured current exceeds the noise level. Samples that have a temperature dependence according to

$$\sigma(T) = \sigma_0 e^{-(T_0/T)^{1/2}} \quad (1)$$

can be attributed to correlated VRH, a process of co-tunneling in the presence of electrostatic disorder caused by trapped charges in the insulating matrix.[23-25] Samples with a temperature dependence of the form

$$\sigma(T) = \sigma_0 e^{-(T_0/T)^{1/4}} \quad (2)$$

follow the so-called Mott-type VRH that corresponds to a finite probability for single-electron tunneling to spatially remote states close to the chemical potential.

Samples 5 and 6, corresponding to a Si/Pt ratio of 1:1 and 3:2, respectively, show correlated VRH (Figure 5a), whereas samples 3 and 8 show Mott-type VRH (Figure 5b). In detail, the measurements show a

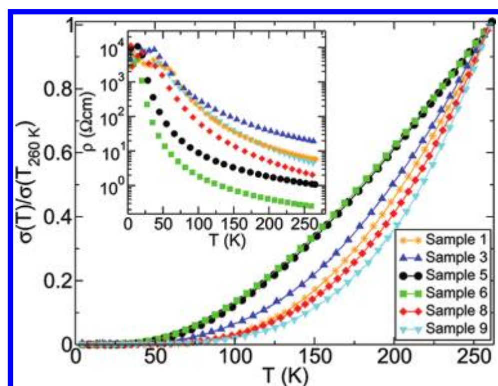

Figure 4. Temperature-dependent conductivity for selected samples 1, 3, 5, 6, 8, and 9 corresponding to Si/Pt ratios of 0, 0.4:1, 1:1, 3:2, 2.4:1, and 2.8:1. The conductivity is shown normalized to its corresponding value at 260 K. In the inset, the absolute values of the temperature-dependent resistivity for the same samples are displayed. All samples show insulating behavior at low temperatures.

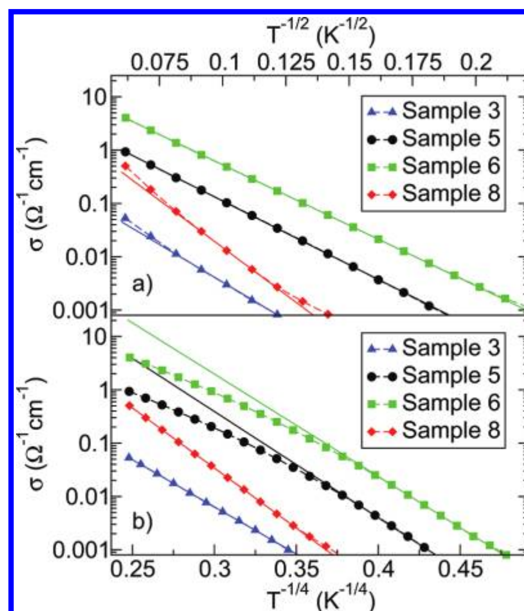

Figure 5. Electrical conductivity plotted logarithmically *versus* (a) $T^{-1/2}$ and (b) $T^{-1/4}$ in the temperature range from 20 to 260 K for selected samples. The solid lines correspond to linear fits of the experimental data according to eq 1 and 2. The measurements show a crossover from Mott-type to correlated VRH and back to Mott-type VRH with growing Si/Pt ratio. Linear fits indicate that (a) samples 5 and 6 follow the Mott-type $T^{-1/4}$ law and (b) samples 3 and 8 show correlated VRH of the type $T^{-1/2}$.

crossover from Mott-type to correlated variable range hopping (VRH) and back to Mott-type VRH with growing Si/Pt ratio. For sample 3 with a Si/Pt ratio of 0.4:1, we observe Mott-type VRH in the temperature range of 66–260 K. With increasing silicon content, a transition to correlated VRH occurs for samples 5 and 6 in the temperature range of 31–260 and 28–260 K with activation temperatures of T_0 = 3035 and 2736 K, respectively. For even higher silicon content, Mott-type VRH is observed again for sample 8 with a Si/Pt ratio of 2.4:1 for temperatures between 73 and 260 K.

TEM Measurements. In order to determine the microstructure and crystallinity of our samples, we performed high-resolution cross-section TEM and diffraction measurements. The analyzed deposits had a nominal thickness of ~100 nm and were grown on a Cu TEM grid with a 30 nm thick carbon membrane using, except for the $Si(SiH_3)_4$ precursor flux, the identical deposition parameters as used for the electrical transport measurements. The $Si(SiH_3)_4$ precursor flux had to be adjusted to obtain the Si/Pt ratios of 1:1, 3:2 and 3:1 as the substrate was altered for the TEM measurements leading to a shift in the Si/Pt ratio toward higher values. In Figure 6, diffraction patterns, as well as their corresponding high-resolution cross-section TEM images, are shown for (a) the silicon-free Pt–C reference, (b) the Si/Pt ratio 1:1, (c) the Si/Pt ratio 3:2, and (d) the Si/Pt ratio 3:1.

The Pt–C reference sample (Figure 6a) shows a nanogranular structure and a diffraction pattern that is consistent with a face-centered cubic structure with a lattice constant of 3.92 Å, in excellent agreement with recent investigations.[26] For increasing silicon content (Figure 6b–d), no additional reflexes occur in the diffraction patterns that would indicate a formation of a crystalline Pt–Si phase. Moreover, the diffraction patterns become more and more diffuse, indicating an increasing amorphous part in the nanogranular structure. Therefore, the degree of crystallinity of the samples decreases with increasing silicon content.

The high-resolution cross-section TEM images (Figure 6a–d, right) display the granular structure of the samples. Although a qualitative structural difference for the different Si/Pt ratios is observable, the grain size cannot be determined from these TEM images.

DISCUSSION

The work presented here—the preparation of binary systems with FEBID—is for the most part uncharted territory. The growth conditions in the FEBID process are far from thermal equilibrium. Therefore, for the system Pt–Si, the central question arises which phases can be formed under these conditions. In a recent experiment by Che *et al.*, the FEBID process was applied with a gas mixture of iron pentacarbonyl ($Fe(CO)_5$) and $MeCpPt(Me)_3$ in order to fabricate crystalline FePt alloy nanorods. A crystalline phase could only be obtained after postannealing of the samples at 600 °C for 2 h.[27] With our experiments on the Pt–Si binary system, we extend the FEBID technique further by simultaneously introducing two precursors $MeCpPt(Me)_3$ and $Si(SiH_3)_4$ through two independent gas-injection systems (GIS). This method allows us to continuously tune the Si/Pt ratio in the deposits.

For sample 1, without any $Si(SiH_3)_4$ precursor flux, the deposits consist of 22% platinum and 78% carbon.

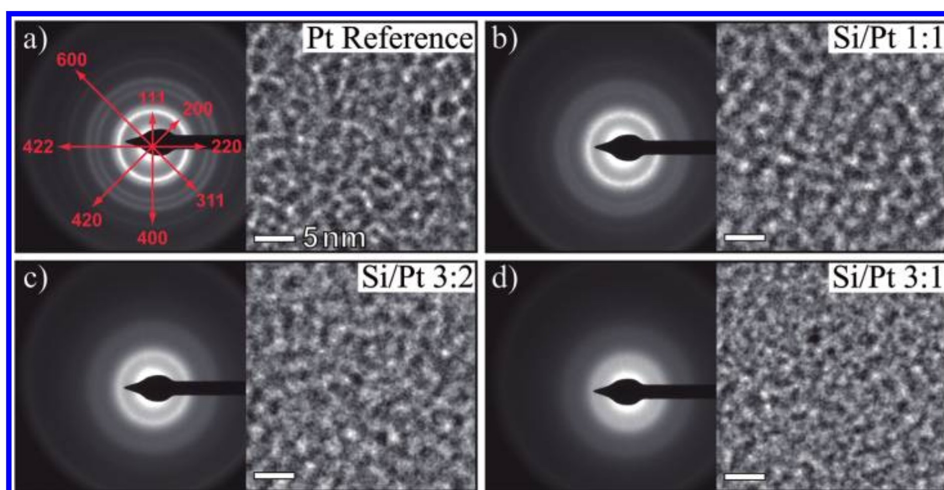

Figure 6. Selected area diffraction patterns and their corresponding high-resolution cross-section TEM images for (a) Pt reference, (b) Si/Pt ratio 1:1, (c) Si/Pt ratio 3:2, and (d) Si/Pt ratio 3:1. The platinum reference sample shows a nanogranular structure and a diffraction pattern that is consistent with fcc platinum. For increasing silicon content, the diffraction patterns become more and more diffuse, indicating an increasing amorphous part in the nanogranular structure.

If we now increase the $Si(SiH_3)_4$ precursor flux, two scenarios for the implementation of silicon into the granular structure of the Pt–C samples are conceivable. On the one hand, silicon can replace carbon in the insulating matrix, which will change the dielectric constant of the matrix and therefore increase the conductivity by influencing the intergrain tunnel coupling.[28] When exposed to air, weakly bonded silicon atoms or silicon atoms with unsaturated bonds in the matrix can be oxidized and form SiO or SiO_2, leading to an increase of the oxygen content as found in the EDX measurements. On the other hand, silicon and platinum can form Pt–Si compounds, leading to a reduction of the number density of platinum nanocrystals. As Pt–Si compounds are well-known for their high conductivity, the conductivity of the samples should then increase, as well. However, which Pt–Si phases are formed will depend on the ratio of the $Si(SiH_3)_4$ and $MeCpPt(Me)_3$ precursor flux during deposition, as well as the deposition parameters. Also an interplay of both processes is possible.

For low silicon contents up to ~8%, the decreasing carbon content in combination with the constant platinum content and the similar curve progression of oxygen and silicon up to sample 3 (Figure 1b) strongly indicate that silicon is integrated into the carbon-rich insulating matrix without influencing the nanogranular structure. Samples with low silicon content display Mott-type VRH, which is observed in strongly disordered systems with localized states. For increasing silicon content, starting from sample 5, the qualitative curve progression of carbon, oxygen, platinum, and silicon in the EDX measurements (Figure 1b) changes significantly. Here the carbon content remains almost constant up to sample 9. In addition, for the samples exposed to air, the oxygen content decreases with increasing silicon content, showing the same qualitative development as platinum. We now speculate that the additional silicon is not integrated into the dielectric matrix but forms a Pt–Si phase. This change in the deposits' growth behavior is supported by the observed reduction of the growth rate starting from sample 5 (Figure 2). The nonmonotonic growth rate can be interpreted as an interplay between two processes. For samples with low silicon content, the integration of silicon into the carbon-rich dielectric matrix leads to an increase in the deposits' height with a maximum of 120 nm for sample 4 due to the larger atomic radius of silicon compared to equally coordinated carbon as well as stronger oxidation effects in the presence of silicon. For samples with higher silicon content, preferentially Pt–Si compound coordinations of the atoms with increased density are formed, leading to a reduction of the growth rate. Furthermore, the observed crossover from Mott-type VRH to correlated VRH, which implies a change in the electronic structure, also supports the change in the deposits' growth behavior. Such a crossover in the electronic transport regimes from Mott to correlated VRH can be observed for materials with a low density of states[29] but is not expected for granular metals. Nevertheless, the formation of short-range order in the hexagonal Pt–Si coordination corresponding to the coordination in the ordered compound Pt_2Si_3 (metastable) might very well lead to an associated granular electronic density of states. This would favor the crossover to correlated VRH. This would also be consistent with the minimum resistivity observed for sample 6 and the lack of long-range crystal coherence evident in the TEM diffraction experiments. This argument is further supported by experiments from Tsaur *et al.*[30−32] They showed that by Xe ion-beam-induced mixing of a platinum silicon interface and postannealing at 400 °C the metastable crystalline Pt_2Si_3 phase could be stabilized. Before the

annealing step, an amorphous Pt_2Si_3 alloy was formed that was then transformed into the crystalline metallic Pt_2Si_3 phase by annealing. On both sides of the stoichiometric proportion 2:3, the Pt_2Si_3 phase formation is hindered leading to the resistivity increase and change of the hopping behavior. Interestingly, at 1:1 ratio, correlated VRH is established again. Pt_1Si_1, on the other hand, is a congruently melting intermetallic compound that shows superconductivity below 0.5 K. Here again we are led to assume that an amorphous Pt_1Si_1 precursor alloy is formed which leads to a granular electronic density of states.

In order to foster the formation of a crystalline Pt_2Si_3 phase in our FEBID experiments, we are planning to post-treat our deposits by electron-beam irradiation.

CONCLUSION

In summary, we have prepared binary systems of Pt−Si by FEBID by simultaneously using the two precursors $MeCpPt(Me)_3$ and, for the first time, neopentasilane $Si(SiH_3)_4$. With growing silicon content in the deposits, electrical transport measurements reveal a crossover from Mott-type to correlated VRH for samples with the Si/Pt ratios of 1:1 and 3:2. For Si/Pt ratios greater than 3:2, the transport regime crosses over to Mott-type VRH again. Taking all experimental results into account, this behavior can be understood as being due to a development of a granularity of the electronic density of states in combination with the formation of an amorphous metallic Pt_1Si_1 and a metastable metallic Pt_2Si_3 phase leading to a maximum in the conductivity for a Si/Pt ratio of 3:2. The differing characteristics of these Si/Pt compositions are also supported by the binary Pt−Si phase diagram.[33] Future work will be directed to a thorough investigation of the properties of other binary FEBID structures, further extending the material base to magnetic alloy nanostructures.

METHODS

FEBID Deposition. The deposits were fabricated by FEBID using a dual-beam SEM/FIB microscope (FEI, Nova Nanolab 600) with a Schottky electron emitter. The microscope is equipped with several GIS. With each GIS, one precursor gas can be introduced into the chamber through a thin capillary (Ø = 0.5 mm) in close proximity to the focus of the electron beam.[34] The two precursors $MeCpPt(Me)_3$ and $Si(SiH_3)_4$ were simultaneously introduced into the chamber. The Pt−Si deposits were grown between 120 nm thick Cr/Au contacts with a separation of ~4 μm. A lift-off process was applied for patterning using UV lithography to define the contacts, which were sputtered onto a 300 nm thick layer of SiO_2 on top of a p-doped silicon (100) substrate. During the deposition, a beam current of 930 pA and an acceleration voltage of 5 kV were applied. The area of the deposits of $1 \times 6\,\mu m^2$ and the deposition time $\Delta t = 60$ s, pitch of 20 nm, and dwell time $t_D = 1\,\mu s$ were kept fixed for all samples. The Si/Pt ratio was altered by changing the $Si(SiH_3)_4$ precursor flux at the focus of the electron beam, while keeping the $MeCpPt(Me)_3$ precursor flux fixed for all depositions. During the deposition process, *in situ* conductance measurements at a fixed bias voltage (10 mV) were performed using a Keithley 2400 source meter.

Transport Measurements. Electrical transport measurements in the temperature range of 1.5−260 K were performed in a ^4He cryostat equipped with a variable temperature insert in combination with a Keithley 2400 source meter. The measurements were performed in a two-probe setup with fixed bias voltage, resulting in an electrical field of 20−40 V/cm. The composition of the different deposits was analyzed by means of energy-dispersive X-ray spectroscopy (EDX) at 5 keV electron beam energy, directly after the deposition and after the electrical transport measurements and exposure of the deposits to air. To determine the resistivity for different Si/Pt ratios, the spatial dimensions of the samples were measured by AFM (Nanosurf easyScan 2) in noncontact mode.

TEM Measurements. For microstructural analysis, transmission electron microscopy (TEM, Tecnai F20) was performed at 200 kV on $1 \times 6\,\mu m^2$ reference samples with different Si/Pt ratios and a thickness of ~100 nm. These were grown on a Cu TEM grid with a 30 nm thick carbon membrane. Diffraction patterns were taken to investigate the possible formation of platinum silicide nanocrystals.

Neopentasilane. In this study, we used $Si(SiH_3)_4$ as a precursor in the FEBID process for the first time. Neopentasilane was synthesized from chlorosilanes donated by Next Step GmbH, Germany. Other chemicals were purchased from Sigma-Aldrich. Products were characterized *via* nuclear magnetic resonance spectroscopy (NMR) experiments using a Bruker Avance 400 spectrometer with deuterated benzene as solvent. Due to the highly pyrophoric character of the neopentasilane, the synthesis and analysis were carried out under nitrogen atmosphere using common Schlenk techniques. For the synthesis of neopentasilane, a Schlenk flask was charged with 10 g (0.018 mol) of dodecachloroneopentasilane, which was prepared according to literature.[35−39] Forty-one milliliters (0.230 mol) of DIBAL-H was added dropwise under stirring, while the reaction flask was cooled in an ice bath. Then, the reaction was allowed to warm to room temperature and stirred for another 5 h. The product was condensed from the reaction mixture into a cooling trap (77 K) at 1 Pa, yielding 2.47 g (90%) of pure neopentasilane. The ^1H NMR signal of the four identical SiH_3 groups was found to be a singlet at 3.41 ppm; the ^{29}Si NMR signals of the primary and the quaternary silicon atoms were found to be at −89.6 and −164.2 ppm, respectively.

Acknowledgment. The authors acknowledge financial support by the NanoNetzwerkHessen (NNH), by the Bundesministerium für Bildung und Forschung (BMBF) under Grant No. 0312031C and the European FP7 project "ALBICAN" under Grant No. 286146. Financial support by the Beilstein-Institut, Frankfurt/Main, Germany within the research collaboration NanoBiC is also gratefully acknowledged.

Supporting Information Available: Additional information on the experimental setup and on *in situ* conductivity measurements during growth of the samples is provided. This material is available free of charge *via* the Internet at http://pubs.acs.org.

REFERENCES AND NOTES

1. Liang, T.; Frendberg, E.; Lieberman, B.; Stivers, A. Advanced Photolithographic Mask Repair Using Electron Beams. *J. Vac. Sci. Technol., B* **2005**, *23*, 3101–3105.
2. Klein, K. L.; Randolph, S. J.; Fowlkes, J. D.; Allard, L. F.; Meyer, H. M.; Simpson, M. L.; Rack, P. D. Single-Crystal Nanowires Grown *via* Electron-Beam-Induced Deposition. *Nanotechnology* **2008**, *19*, 345705.
3. Danelon, C.; Santschi, C.; Brugger, J.; Vogel, H. Fabrication and Functionalization of Nanochannels by Electron-Beam-Induced Silicon Oxide Deposition. *Langmuir* **2006**, *22*, 10711–10715.

4. Gabureac, M.; Bernau, L.; Utke, I.; Boero, G. Granular Co-C Nano-Hall Sensors by Focused-Beam-Induced Deposition. *Nanotechnology* **2010**, *21*, 115503.
5. Fernández-Pacheco, A.; De Teresa, J. M.; Cordoba, R.; Ibarra, M. R.; Petit, D.; Read, D. E.; O'Brien, L.; Lewis, E. R.; Zeng, H. T.; Cowburn, R. P. Domain Wall Conduit Behavior in Cobalt Nanowires Grown by Focused Electron Beam Induced Deposition. *Appl. Phys. Lett.* **2009**, *94*, 192509.
6. Serrano-Ramón, L.; Córdoba, R.; Rodríguez, L. A.; Magén, C.; Snoeck, E.; Gatel, C.; Serrano, I.; Ibarra, M. R.; De Teresa, J. M. Ultrasmall Functional Ferromagnetic Nanostructures Grown by Focused Electron-Beam-Induced Deposition. *ACS Nano* **2011**, *5*, 7781–7787.
7. Schwalb, C. H.; Grimm, C.; Baranowski, M.; Sachser, R.; Porrati, F.; Reith, H.; Das, P.; Muller, J.; Volklein, F.; Kaya, A.; Huth, M. A Tunable Strain Sensor Using Nanogranular Metals. *Sensors* **2010**, *10*, 9847–9856.
8. Beloborodov, I. S.; Lopatin, A. V.; Vinokur, V. M.; Efetov, K. B. Granular Electronic Systems. *Rev. Mod. Phys.* **2007**, *79*, 469–518.
9. Porrati, F.; Sachser, R.; Schwalb, C. H.; Frangakis, A. S.; Huth, M. Tuning The Electrical Conductivity of Pt-Containing Granular Metals by Postgrowth Electron Irradiation. *J. Appl. Phys.* **2011**, *109*, 063715.
10. Efetov, K. B.; Tschersich, A. Transition from Insulating to Non-insulating Temperature Dependence of the Conductivity in Granular Metals. *Europhys. Lett.* **2002**, *59*, 114–120.
11. Porrati, F.; Sachser, R.; Strauss, M.; Andrusenko, I.; Gorelik, T.; Kolb, U.; Bayarjargal, L.; Winkler, B.; Huth, M. Artificial Granularity in Two-Dimensional Arrays of Nanodots Fabricated by Focused-Electron-Beam-Induced Deposition. *Nanotechnology* **2010**, *21*, 375302.
12. Sachser, R.; Porrati, F.; Huth, M. Hard Energy Gap and Current-Path Switching in Ordered Two-Dimensional Nanodot Arrays Prepared by Focused Electron-Beam-Induced Deposition. *Phys. Rev. B* **2009**, *80*, 195416.
13. Sachser, R.; Porrati, F.; Schwalb, C. H.; Huth, M. Evidence for Universal Conductance Correction in a Tunable Strongly Coupled Nanogranular Metal. *Phys. Rev. Lett.* **2011**, *107*, 206803.
14. Fernández-Pacheco, A.; De Teresa, J. M.; Córdoba, R.; Ibarra, M. R. Metal-Insulator Transition in Pt-C Nanowires Grown by Focused-Ion-Beam-Induced Deposition. *Phys. Rev. B* **2009**, *79*, 174204.
15. Huth, M.; Klingenberger, D.; Grimm, C.; Porrati, F.; Sachser, R. Conductance Regimes of W-Based Granular Metals Prepared by Electron Beam Induced Deposition. *New J. Phys.* **2009**, *11*, 033032.
16. Liu, Y.; Haviland, D. B.; Nease, B.; Goldman, A. M. Insulator-to-Superconductor Transition in Ultrathin Films. *Phys. Rev. B* **1993**, *47*, 5931–5946.
17. Markovic, N.; Christiansen, C.; Mack, A. M.; Huber, W. H.; Goldman, A. M. Superconductor-Insulator Transition in Two Dimensions. *Phys. Rev. B* **1999**, *60*, 4320–4328.
18. Frydman, A.; Naaman, O.; Dynes, R. C. Universal Transport in Two-Dimensional Granular Superconductors. *Phys. Rev. B* **2002**, *66*, 052509.
19. Zhang, S. L.; Ostling, M. Metal Silicides in CMOS Technology: Past, Present, and Future Trends. *Crit. Rev. Solid State Mater. Sci.* **2003**, *28*, 1–129.
20. Chen, L. J. Metal Silicides: An Integral Part of Microelectronics. *JOM* **2005**, *57*, 24–30.
21. Botman, A.; de Winter, D. A. M.; Mulders, J. J. L. Electron-Beam-Induced Deposition of Platinum at Low Landing Energies. *J. Vac. Sci. Technol., B* **2008**, *26*, 2460–2463.
22. Porrati, F.; Sachser, R.; Huth, M. The Transient Electrical Conductivity of W-Based Electron-Beam-Induced Deposits during Growth, Irradiation and Exposure to Air. *Nanotechnology* **2009**, *20*, 195301.
23. Beloborodov, I. S.; Lopatin, A. V.; Hekking, F. W. J.; Fazio, R.; Vinokur, V. M. Thermal Transport in Granular Metals. *Europhys. Lett.* **2005**, *69*, 435–441.
24. Feigel'man, M. V.; Ioselevich, A. S. Variable-Range Cotunneling and Conductivity of a Granular Metal. *JETP Lett.* **2005**, *81*, 277–283.
25. Tran, T. B.; Beloborodov, I. S.; Lin, X. M.; Bigioni, T. P.; Vinokur, V. M.; Jaeger, H. M. Multiple Cotunneling in Large Quantum Dot Arrays. *Phys. Rev. Lett.* **2005**, *95*, 076806.
26. Li, J. T.; Toth, M.; Dunn, K. A.; Thiel, B. L. Interfacial Mixing and Internal Structure of Pt-Containing Nanocomposites Grown by Room Temperature Electron Beam Induced Deposition. *J. Appl. Phys.* **2010**, *107*, 103540.
27. Che, R. C.; Takeguchi, M.; Shimojo, M.; Zhang, W.; Furuya, K. Fabrication and Electron Holography Characterization of FePt Alloy Nanorods. *Appl. Phys. Lett.* **2005**, *87*, 223109.
28. Huth, M. Granular Metals: From Electronic Correlations to Strain-Sensing Applications. *J. Appl. Phys.* **2010**, *107*, 113709.
29. Liu, H.; Pourret, A.; Guyot-Sionnest, P. Mott and Efros-Shklovskii Variable Range Hopping in CdSe Quantum Dots Films. *ACS Nano* **2010**, *4*, 5211–5216.
30. Tsaur, B. Y.; Mayer, J. W.; Tu, K. N. Ion-Beam-Induced Metastable Pt_2Si_3 Phase I. Formation, Structure, and Properties. *J. Appl. Phys.* **1980**, *51*, 5326–5333.
31. Tsaur, B. Y.; Mayer, J. W.; Graczyk, J. F.; Tu, K. N. Ion-Beam-Induced Metastable Pt_2Si_3 Phase II. Kinetics and Morphology. *J. Appl. Phys.* **1980**, *51*, 5334–5341.
32. Graczyk, J. F.; Tu, K. N.; Tsaur, B. Y.; Mayer, J. W. Ion-Beam-Induced Metastable Pt_2Si_3 Phase III. Structure and Diffusion in Amorphous Pt_2Si_3. *J. Appl. Phys.* **1982**, *53*, 6772–6780.
33. Okamoto, H. Pt–Si (Platinum–Silicon). *J. Phase Equilib.* **1995**, *16*, 286–287.
34. Klingenberger, D.; Huth, M. Modular Ultrahigh Vacuum-Compatible Gas-Injection System with an Adjustable Gas Flow for Focused Particle Beam-Induced Deposition. *J. Vac. Sci. Technol., A* **2009**, *27*, 1204–1210.
35. Kaczmarczyk, A.; Urry, G. A New Synthesis for Hexasilicon Tetradecachloride. *J. Am. Chem. Soc.* **1960**, *82*, 751–752.
36. Kaczmarczyk, A.; Millard, M.; Urry, G. A New Pentasilicon Dodecachloride, Si_5Cl_{12}. *J. Inorg. Nucl. Chem.* **1961**, *17*, 186–188.
37. Kaczmarczyk, A.; Millard, M.; Nuss, J. W.; Urry, G. The Preparation and Some Properties of a New Pentasilicon Dodecachloride, Si_5Cl_{12}. *J. Inorg. Nucl. Chem.* **1964**, *26*, 421–425.
38. Nuss, J. W.; Urry, G. On the Structures of Pentasilicon Dodecachloride, Si_5Cl_{12}, and Hexasilicon Tetradecachloride, Si_6Cl_{14}. *J. Inorg. Nucl. Chem.* **1964**, *26*, 435–444.
39. Urry, G. Systematic Synthesis in Polysilane Series. *Acc. Chem. Res.* **1970**, *3*, 306–312.